

Experimental realization of on-chip few-photon control around exceptional points

Received: 1 May 2023

Accepted: 31 October 2024

Published online: 14 November 2024

 Check for updates

Pengtao Song^{1,2,14}, Xinhui Ruan^{1,2,3,14}, Haijin Ding³, Shengyong Li³, Ming Chen¹, Ran Huang¹, Le-Man Kuang¹, Qianchuan Zhao³, Jaw-Shen Tsai^{4,5}, Hui Jing¹, Lan Yang⁶, Franco Nori^{4,7,8}, Dongning Zheng^{2,9,10}✉, Yu-xi Liu¹¹, Jing Zhang^{12,13}✉ & Zhihui Peng^{1,10}✉

Non-Hermitian physical systems have attracted considerable attention in recent years for their unique properties around exceptional points (EPs), where the eigenvalues and eigenstates of the system coalesce. Phase transitions near exceptional points can lead to various interesting phenomena, such as unidirectional wave transmission. However, most of those studies are in the classical regime and whether these properties can be maintained in the quantum regime is still a subject of ongoing studies. Using a non-Hermitian on-chip superconducting quantum circuit, here we observe a phase transition and the corresponding exceptional point between the two phases. Furthermore, we demonstrate that unidirectional microwave transmission can be achieved even in the few-photon regime within the broken symmetry phase. This result holds some potential applications, such as on-chip few-photon microwave isolators. Our study reveals the possibility of exploring the fundamental physics and practical quantum devices with non-Hermitian systems based on superconducting quantum circuits.

Non-Hermitian physical systems with exceptional points^{1–5} (EPs) have attracted considerable attention in recent years. The coalescence of eigenvalues and eigenstates of the non-Hermitian Hamiltonian around EPs leads to various interesting properties and numerous applications, such as unidirectional transmission and invisibility^{6–12}, chiral behavior¹³, control of lasers^{14–17} or electromagnetic waves¹⁸, high-precision sensors^{19–22}, and topological energy transfer^{3,23}. While non-Hermitian physics has been studied extensively in classical systems, the quantum behavior of non-Hermitian systems is not fully understood and there is still much to be explored in the quantum realm.

Although there has been interesting work to mimic gain-loss-balance mechanisms in two-level systems (e.g., superconducting quantum circuits^{24,25}, nitrogen-vacancy centers in diamonds²⁶ and trapped ions²⁷), various interesting problems related to quantum non-Hermitian systems in the few-photon regime are still left open^{28,29}. One interesting topic is unidirectional control of light in the few-photon regime for non-Hermitian systems. Such kinds of quantum nonreciprocal effects are very helpful for constructing quantum devices³⁰, such as quantum diodes³¹ and quantum circulators³², which are key components for quantum information processing. Although it

¹Key Laboratory of Low-Dimensional Quantum Structures and Quantum Control of Ministry of Education, Department of Physics and Synergetic Innovation Center of Quantum Effects and Applications, Hunan Normal University, Changsha, China. ²Institute of Physics, Chinese Academy of Sciences, Beijing, China. ³Department of Automation, Tsinghua University, Beijing, China. ⁴Center for Quantum Computing, RIKEN, Saitama, Japan. ⁵Graduate School of Science, Tokyo University of Science, 1–3 Kagurazaka, Shinjuku, Tokyo, Japan. ⁶Department of Electrical and Systems Engineering, Washington University, St. Louis, MO, USA. ⁷Theoretical Quantum Physics Laboratory, Cluster for Pioneering Research, RIKEN, Saitama, Japan. ⁸University of Michigan, Ann Arbor, MI, USA. ⁹School of Physical Sciences, University of Chinese Academy of Sciences, Beijing, China. ¹⁰Hefei National Laboratory, Hefei, China. ¹¹School of Integrated Circuits, Tsinghua University, Beijing, China. ¹²School of Automation Science and Engineering, Xi'an Jiaotong University, Xi'an, China. ¹³MOE Key Lab for Intelligent Networks and Network Security, Xi'an Jiaotong University, Xi'an, China. ¹⁴These authors contributed equally: Pengtao Song, Xinhui Ruan.

✉ e-mail: dzheng@iphy.ac.cn; zhangjing2022@xjtu.edu.cn; zhihui.peng@hunnu.edu.cn

is well known that non-reciprocal wave propagations can be achieved by breaking the symmetries of non-Hermitian physical systems in the vicinity of the exceptional point, it is challenging to show such kinds of symmetry breaking in the few-photon regime, because the enhanced quantum fluctuations at the exceptional point will disrupt this process.

Demonstrating nonreciprocity in the few-photon regime requires strong nonlinearity, which is quite difficult to achieve in optical systems. This issue could be solved by using superconducting systems, in which strong nonlinearity has been successfully demonstrated at the single-photon level in the microwave frequency regime³³. Superconducting quantum information processing has made great progresses in recent years^{34–37}. Highly-efficient widely-tunable on-demand single-photon sources and highly-efficient single-photon detectors in the microwave-frequency regime have been realized in superconducting quantum systems^{38–40}. With the quantum state transfer by a single microwave photon between two superconducting qubits housed in two refrigerators separated apart by 5 meters, it is possible to realize a microwave quantum network and distributed superconducting quantum computing⁴¹. There has been some research on non-Hermitian phenomena in superconducting circuits^{42–44}. However, the control of the transmission of a single microwave photon on a chip is still ongoing research, and is one of the crucial open problems for quantum networks.

In this work, we construct a non-Hermitian system using a superconducting circuit consisting of two cavities and three tunable-gap flux qubits. The two cavities have different decay rates and nearly identical resonance frequencies, with tunability within a range of a few

tens of MHz. The effective coupling strength between the cavities can be tuned by a quantum coupler, implemented here as a tunable-gap flux qubit. Using this non-Hermitian system, we observe the phase transitions and the corresponding exceptional points. The qubits introduce additional nonlinearity to the two cavities, enabling the generation of unidirectional microwave transmission. By tuning the effective coupling strength between the cavities and the input photon numbers, we investigate the switchable unidirectional transmission of the system at the few-photon level.

Results

Experimental setup

Our experiment is carried out in a dilution refrigerator with a base temperature of about 28 mK. As shown in Fig. 1a–c, the device consists of two superconducting coplanar waveguide (CPW) cavities (marked as Cavity *a* and Cavity *b*, respectively) that are capacitively coupled to a tunable-gap flux qubit (working as a quantum coupler and marked as qubit Q_C) with two nominal identical capacitors (see Fig. 1b, c). Tunable coupling between two CPW cavity modes or two CPW cavities based on a flux qubit have been demonstrated^{45,46}. The Hamiltonian of a qubit coupled to a cavity in the dispersive regime is $H \approx \hbar(\omega_c + \tilde{\chi}\sigma_z)a^\dagger a + \hbar(\omega_q + \tilde{\chi})\sigma_z/2$, where ω_c is the cavity frequency, ω_q is the qubit transition frequency, $\tilde{\chi} = g_0^2/\delta$ is the qubit-state-dependent dispersive cavity shift³³, $\delta = |\omega_q - \omega_c| \gg g_0$, g_0 is the coupling strength between the qubit and the cavity, $\sigma_z = |0\rangle\langle 0| - |1\rangle\langle 1|$ with the ground $|0\rangle$ and excited $|1\rangle$ states of the qubit, and a^\dagger and a are the creation and annihilation operators of the cavity, respectively. The

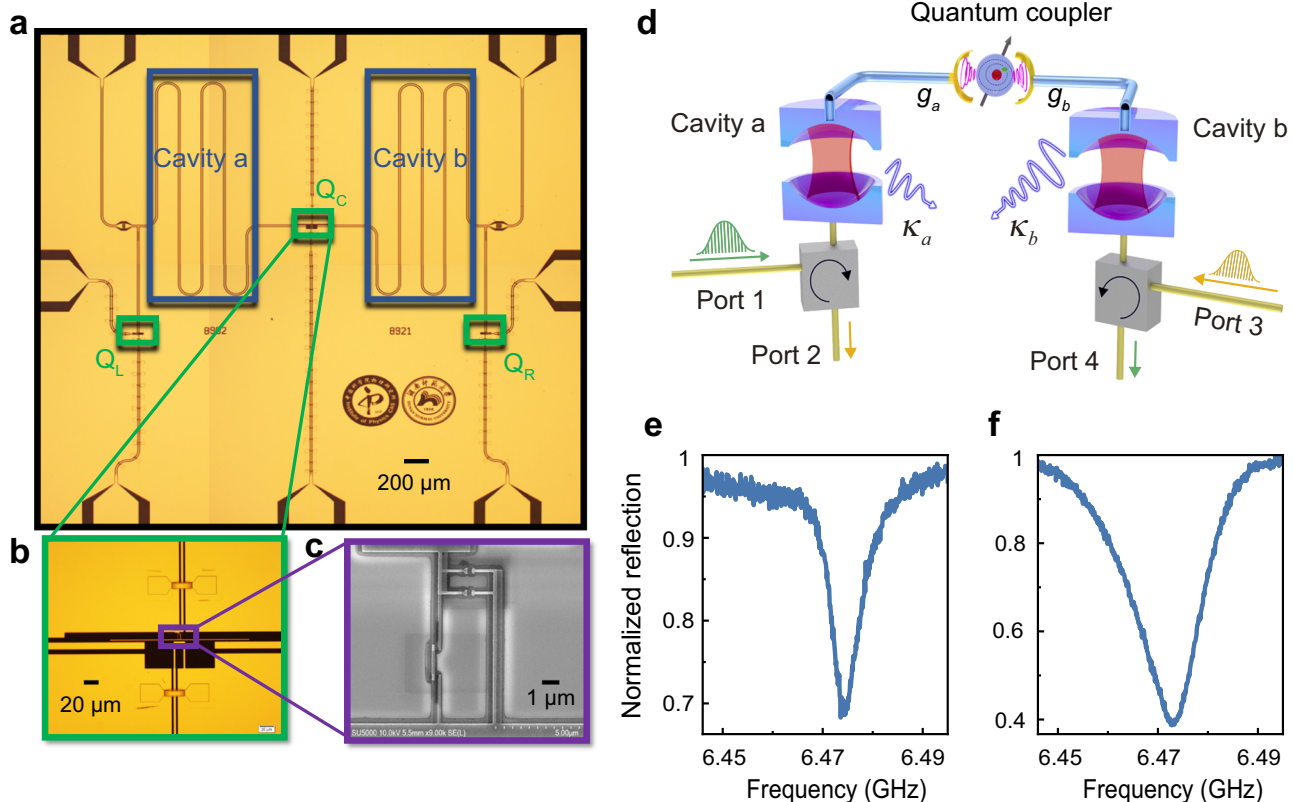


Fig. 1 | Schematic diagram of the superconducting quantum chip. a Optical micrograph of the coupling qubit and the two indirectly-coupled coplanar waveguide (CPW) cavities. Two CPW cavities have the same resonant frequency of $\omega_a/2\pi \approx \omega_b/2\pi \approx 6.474$ GHz but different decay rates of $\kappa_a/2\pi = 7.7$ MHz and $\kappa_b/2\pi = 20.9$ MHz. There are three tunable-gap flux qubits. The left (right) qubit Q_L (Q_R) only couples to the left (right) CPW cavity and works as a cavity frequency shifter to tune the resonant frequency of the left (right) cavity. The central qubit Q_C

couple to the two cavities as a quantum coupler to tune the coupling strength between the two cavities. Optical micrograph (b) and scanning electron micrograph (c) of the coupling flux qubit. d Equivalent schematic diagram in which two cavities couple with each other by a quantum coupler. Each cavity is connected to a circulator for extending ports. Reflection spectra of the left high-Q cavity (e) and the right low-Q cavity (f) that display Lorentzian lineshapes detected at low probing power to keep the average photon numbers inside the cavities less than one.

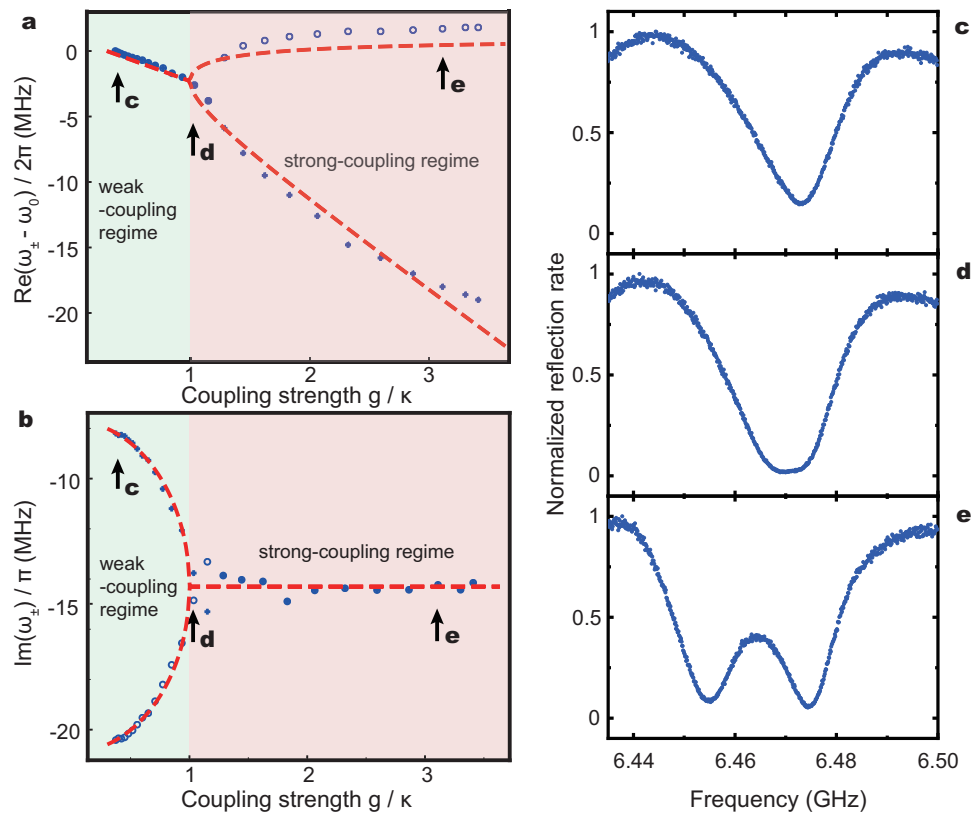


Fig. 2 | Bifurcation diagram of the supermodes in the vicinity of the exceptional points. a The real part of the supermodes (frequency). **b** the imaginary part of the supermodes (decay rate). **a, b** The blue circles and crosses represent the experimental data and the dashed lines represent the theoretical curves. Normalized reflection spectra from the right low- Q cavity with different coupling strength g . **(c)** Before the exceptional point ($g/\kappa = 0.29$) in which two supermodes overlap with

each other but with different decay rates. **(d)** In the vicinity of the exceptional point ($g/\kappa = 1.04$) in which two supermodes are degenerate. **(e)** After the exceptional point ($g/\kappa = 3.11$) in which two supermodes are splitting. The applied probing power is low enough to keep $\langle n_a \rangle \approx 0.06$ with a precision better than ± 3 dB inside the high- Q cavity.

eigenfrequencies of the two CPW cavities (ω_a for cavity a and ω_b for cavity b , respectively) can be shifted for a few tens of MHz in the dispersive coupling regime, because the cavities are capacitively coupled to other two auxiliary tunable-gap flux qubits (working as cavity frequency shifters and marked as qubit Q_L and qubit Q_R , respectively). Therefore, it is easy to control the detuning frequency between the frequency of the qubit Q_L and the frequency of the cavity a , and that of the qubit Q_R and the cavity b , respectively. In this way, ω_a and ω_b are tuned to be equal to each other, although the bare eigenfrequencies of the cavities are deviated for few MHz due to the limitation of fabrication. As shown in Fig. 1d, we can apply probing signals through port 1 (port 3) of the left (right) circulator and detect the output signals from port 2 or port 4. It yields four complex elements S_{ji} of the scattering matrix S , where $i \in \{1, 3\}$ and $j \in \{2, 4\}$. For example, the normalized S -matrix S_{21} (S_{43}) is the reflection coefficient of the left (right) cavity, and S_{41} (S_{23}) is the forward (backward) transmission coefficient. The left cavity (cavity a) supports a high- Q cavity mode a with eigenfrequency $\omega_a/2\pi \approx 6.474$ GHz and decay rate $\kappa_a/2\pi \approx 7.7$ MHz, and the right one (cavity b) supports a low- Q cavity mode b with the same eigenfrequency $\omega_b/2\pi \approx 6.474$ GHz but different decay rate $\kappa_b/2\pi \approx 20.9$ MHz (see Fig. 1e, f).

The difference between the decay rates of the two CPW cavities are large enough, such that we can tune the effective coupling strength between the two cavities by changing the transition frequency of the quantum coupler to operate the system in three regimes, i.e., before, after, and in the vicinity of the exceptional point. The coupling flux qubit can be considered as a two-level artificial atom (see Fig. 1d) with transition frequency modulated by the injected external magnetic flux

Φ_m in the main loop or Φ_α in the α loop⁴⁵. It works as a quantum coupler to adjust the effective coupling strength between the two cavities (see section 2 of the Supplementary materials). The effective eigenfrequency of the flux qubit is $\Delta_{\text{eff}} = \sqrt{(2I_p \delta\Phi)^2 + [\Delta(\Phi_\alpha)]^2}$, where $\delta\Phi = \Phi_m - \Phi_0/2$ and Φ_0 is the flux quantum, I_p is the persistent current in the qubit loop, $\Delta(\Phi_\alpha)/h \geq 2.0$ GHz is the energy gap of the flux qubit which can be turned up by Φ_α . By adiabatically eliminating the degree of freedom of the coupling flux qubit, the effective coupling strength between the two cavities is $g = (2\Delta_q g_a g_b) / (\gamma_\perp^2 + \Delta_q^2)$, where γ_\perp is the relaxation rate of the qubit, $\Delta_q = \Delta_{\text{eff}} - \omega_a$ and $g_a = g_b = 71$ MHz are the coupling strength between the cavity a (b) and the coupling qubit, respectively.

Observation of the exceptional point

As shown in Fig. 2, the two cavity modes a and b generate two supermodes a_\pm with complex eigenfrequencies $\omega_\pm \approx \omega_0 - g - i\chi \pm \beta$, where $\omega_a = \omega_b = \omega_0$, $\chi = (\kappa_a + \kappa_b)/4$, $\beta = \sqrt{g^2 - \kappa^2}$, and $\kappa = (\kappa_b - \kappa_a)/4$. The point $g = \kappa$ corresponds to an EP at which both the eigenvalues and the eigenvectors coalesce. The applied probing power P is sufficiently low to keep the average photon numbers $\langle n_i \rangle = P/h\omega_i\kappa_i$ ($i = a, b$) inside the cavity less than one. It can be calibrated by the ac-Stark shift, which is the transition frequency shift of the qubit depending on $\langle n_a \rangle$, i.e., $\Delta\omega_L = 2\langle n_a \rangle g_a^2/\delta$ (see section 1 of the Supplementary materials). After fitting the normalized reflection spectra ($|S_{21}|^2$ or $|S_{43}|^2$) with the Lorentzian curves, we obtain the resonance frequencies (the real parts of) and the decay rates (the imaginary parts of) of the supermodes. As

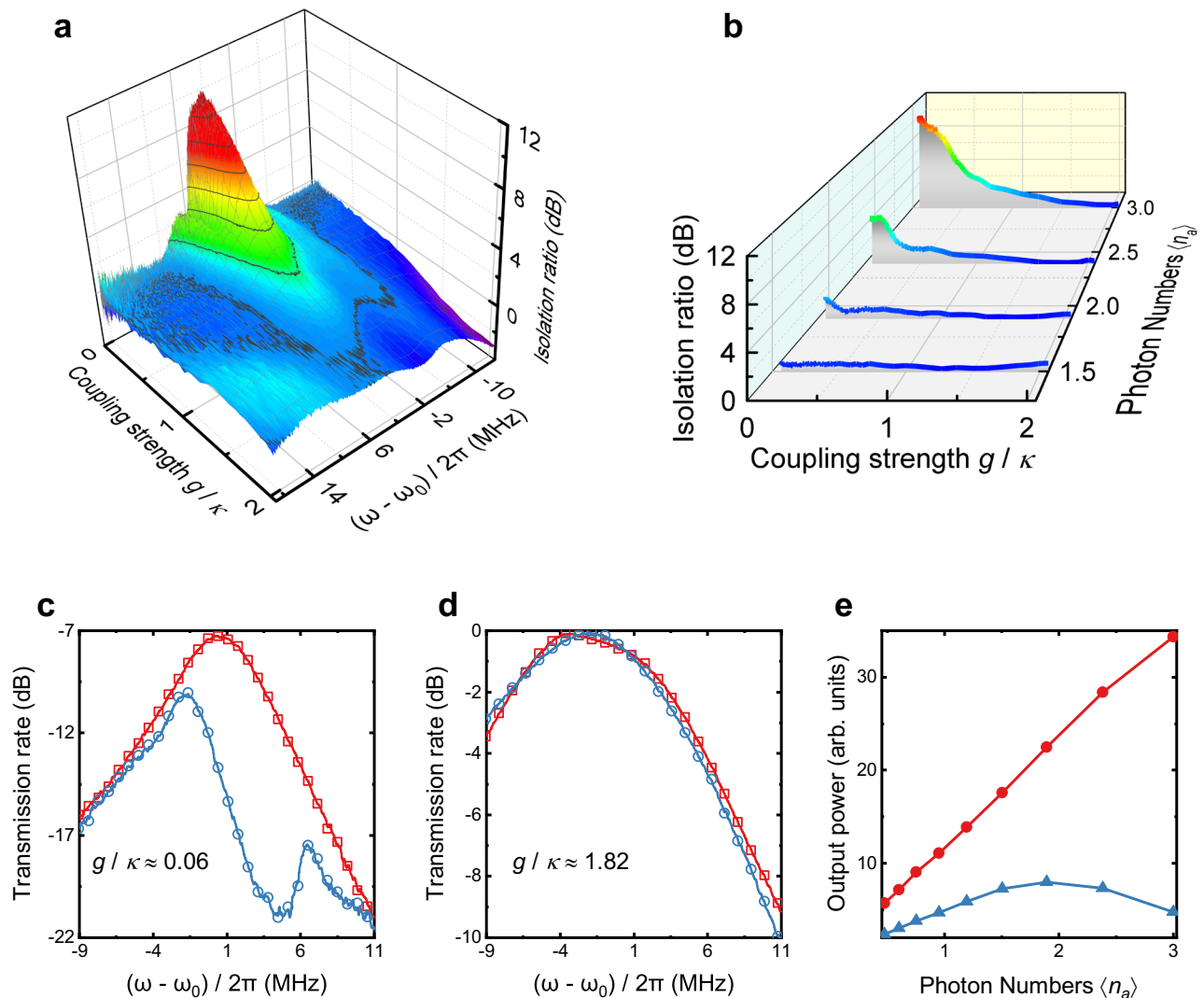


Fig. 3 | Few-photon nonreciprocity. **a** Isolation ratio versus the effective coupling strength g and the detuning frequency between the frequency ω of the probe field and the frequency ω_0 of the cavity mode with $\langle n_a \rangle \approx 3$. **b** Isolation ratio versus effective coupling strength g/κ and the average photon numbers $\langle n_a \rangle$ inside the cavity with $(\omega - \omega_0)/2\pi \approx 2.7$ MHz. **c** Comparison of forward (blue, $1 \rightarrow 4$ in Fig. 1a) and backward (red, $3 \rightarrow 2$ in Fig. 1a) transmission rates in the weak-coupling regime. **d** Same as **c** in the strong-coupling regime. The transmission rates in **c** and

d are defined as $10 \log(V_{\text{out}}^2/V_{\text{in}}^2)$ and have been normalized, where V_{in} and V_{out} are the input and output complex amplitudes of the probing fields. **e** The forward output power versus the average photon numbers $\langle n_a \rangle$ with $(\omega - \omega_0)/2\pi \approx 2.7$ MHz. The red circle data are measured with effective coupling strength $g/\kappa \approx 2.70$. The blue triangle data are measured with coupling strength $g/\kappa \approx 0.09$. The sweep direction for **a–e** is from low frequency to high frequency, from forward to backward, and from low power to high power.

shown in Fig. 2a, b, in the strong-coupling regime $g > \kappa$, the two supermodes a_{\pm} have the same damping rate 2χ but different resonance frequencies $\omega_0 - g \pm \beta$. The additional frequency shift from ω_0 to $\omega_0 - g$ for supermodes is induced by the interaction between the quantum coupler (the qubit Q_C) and the cavity modes in the strong dispersive limit, and thus causes the asymmetric frequency evolution in Fig. 2a. In the weak-coupling regime $g < \kappa$, the resonance frequencies of the two supermodes will be degenerate as ω_0 , while the damping rates of the two supermodes $2\chi \mp i\beta$ will be different. In our experiments, the damping rate κ is kept fixed and the effective coupling strength between the two cavity modes can be tuned by varying the bias flux $\delta\Phi$ in the main loop of the qubit Q_C , by which we can operate the system in the above three different regimes. Fig. 2c–e show the output spectra of the supermodes in three different regimes, in which the cavity modes a and b have fixed decay rates but different effective coupling strengths $g/\kappa = 0.29, 1.04$, and 3.11 , respectively, where $\kappa = 2\pi \times 3.3$ MHz. It is shown in Fig. 2d that the supermodes are degenerate in the vicinity of the exceptional point such that $g \approx \kappa$.

Nonreciprocal transmission at the few-photon level

Strong nonlinearity can result in nonreciprocal transmission of photons. In our system, the auxiliary and coupling qubits will induce third-order nonlinear terms to the cavity modes. However, since the frequency detunings between the qubits and cavity modes are large in our experiments, the coefficients of the third-order nonlinear terms are of the order of several kHz when the system is away from EP, and thus is too weak to induce nonreciprocal transmission of photons (see section 3 of the Supplementary materials). Fortunately, in the weak-coupling regime and in the vicinity of EP, the supermodes are localized in the high- Q cavity and thus the nonlinearity of the system is efficiently enhanced. This enhanced nonlinearity enables nonreciprocal transmission of photons in the weak-coupling regime (see Fig. 3c). In fact, in the experiments, we apply probing fields with average photon numbers $\langle n_a \rangle \approx 3$ inside the high- Q cavity from port 1 (forward with a transmittance T_F) and port 3 (backward with a transmittance T_B) respectively. The backward output field is stronger than the forward one when the effective coupling strength is weak. However, this nonreciprocal effect is suppressed when the effective coupling strength

between the two cavities is strong enough to enter the strong-coupling regime (Fig. 3d). We demonstrate the nonreciprocal transmission of photons under different coupling strengths, and the maximum isolation ratio defined as $I = 10 \log(T_B/T_F)$ can be up to 10.1 dB with $\langle n_a \rangle \approx 3$ (see Fig. 3a). It is shown in Fig. 3e that the forward output power will increase nonlinearly with the increase of average photon numbers $\langle n_a \rangle$ in the weak-coupling regime, while it will increase linearly in the strong coupling regime.

We also study the isolation ratio depending on the average photon number $\langle n_a \rangle$ inside the high- Q cavity (see Fig. 3b). As we mentioned earlier, the maximum isolation ratio of around 10.1 dB appears in the weak-coupling regime for $\langle n_a \rangle \approx 3$. In the following analysis, we focus on the variation of this maximum value as a function of $\langle n_a \rangle$. In Fig. 3b, the isolation ratio decreases when reducing $\langle n_a \rangle$ and the nonreciprocal transmission phenomenon becomes nearly invisible when we keep $\langle n_a \rangle < 1.5$. The reason is that the nonlinearity of the cavity modes and the amplification of the nonlinearity induced by the EP phenomenon decrease simultaneously with decreasing $\langle n_a \rangle$. Due to the strong nonlinearity of the superconducting quantum circuits at few-photon regime, there is still obvious nonreciprocal transmission effect when we keep $\langle n_a \rangle \approx 2$ (corresponding to the input power less than -122 dBm on chip), which are much smaller than that shown in the classical PT -symmetric system¹¹.

Discussion

We have observed the exceptional points and demonstrated nonreciprocal behavior, i.e., unidirectional transmission of microwave at a few-photon level, in a non-Hermitian superconducting coupled-cavities system with a tunable quantum coupler. When the system is in the weak-coupling regime, the isolation ratio of unidirectional transmission can achieve 10.1 dB, while almost zero isolation ratio is observed in the strong-coupling regime. Our device can be a switchable few-photon isolator by tuning the effective coupling strength between the two coupled-cavities using an external magnetic field. This switchable few-photon isolator has potential applications for the transmission of quantum information.

Methods

The System Hamiltonian

Using Jaynes-Cummings-type description, the total Hamiltonian of the system shown in Fig. 1d is

$$H_c = \omega_a a^\dagger a + \omega_b b^\dagger b + \omega_q \sigma_+ \sigma_- + g_a (a^\dagger \sigma_- + a \sigma_+) + g_b (b^\dagger \sigma_- + b \sigma_+) \quad (1)$$

where $g_a (g_b)$ is the coupling strength between the cavity mode $a (b)$ and the central flux qubit. In our experiment, $g_a \approx g_b$ are the resonance frequencies of the two cavities and the central qubit. By applying adiabatic elimination to the central qubit, we obtain the system's effective Hamiltonian as

$$H_{eff} = \left(\omega_a - g - \frac{i\kappa_a}{2} \right) a^\dagger a + \left(\omega_b - g - \frac{i\kappa_b}{2} \right) b^\dagger b - g(ab^\dagger + a^\dagger b) + \mu_{kerr} (a^\dagger a a^\dagger a + b^\dagger b b^\dagger b), \quad (2)$$

where $\kappa_a (\kappa_b)$ is the decay rate of cavity mode $a (b)$. The effective coupling strength between the two cavity modes g and the effective self-Kerr coefficient μ_{kerr} can be written as

$$g = \frac{\Delta_q g_a g_b}{\Delta_q^2 + \gamma_\perp^2}, \quad (3)$$

$$\mu_{kerr} = \frac{4g_{a(b)}^4 \Delta_q \gamma_\perp}{\gamma_{\parallel} (\Delta_q^2 + \gamma_\perp^2)^2}. \quad (4)$$

Here, $\Delta_q = \omega_q - \omega_a$ and $\gamma_\perp = \gamma_{\parallel}/2 + \gamma_\phi$ is the central qubit's total relaxation rate formed by its depolarizing rate γ_{\parallel} and its dephasing rate γ_ϕ .

At zero detuning ($\omega_a = \omega_b = \omega_0$), The eigenvalues of linear terms in Eq. (2) are

$$\omega_{\pm} = \omega_0 - g - \frac{i}{4}(\kappa_a + \kappa_b) \pm \sqrt{g^2 - \frac{(\kappa_a - \kappa_b)^2}{16}}. \quad (5)$$

It can be shown that there is an exceptional point (EP) at $g = \kappa \equiv |\kappa_a - \kappa_b|/4$. The above calculation details can be found in Section 2 of the supplementary materials.

Device fabrication

The superconducting quantum chip is fabricated using a well-established multi-layer thin-film process, featuring a four-layer structure. Electron-beam lithography is employed for the Josephson junction layer, while optical lithography is used for the other layers. The fabrication process begins by depositing a 100 nm aluminum layer on a sapphire substrate, followed by etching the aluminum to form the coplanar waveguide (CPW) cavities and control lines using an aluminum etchant. Next, a 60 nm gold layer is deposited to serve as markers for e-beam alignment. For the Josephson junctions (flux qubit), we use a standard double-angle evaporation process⁴⁷, depositing 40 nm of aluminum at 20° and 60 nm at -20°. Finally, air-bridges are fabricated above the transmission lines and the control lines to minimize crosstalk between them⁴⁸. The primary challenge in this fabrication process lies in the numerous steps involved, where even a single error at any stage can result in the failure of the entire fabrication.

Measurement

We use a four-port vector network analyzer (VNA) to simultaneously measure the reflection spectra and transmission spectra of the system. We can obtain resonant frequencies and decay rates of the two bare cavities through the reflection spectra when the transition frequencies of the qubits are far away from the cavities. We can apply external magnetic field in α loop to make the transition frequency between the ground state and the excited state of the qubit $Q_L (Q_R)$ resonant with the cavity a (cavity b), respectively. As shown in Fig. S2 in the supplementary materials, we scan the normalized amplitudes of the reflection coefficients ($|S_{21}|$ and $|S_{43}|$) around the resonant frequency of the two cavities as functions of the probing frequency and flux bias $\delta\Phi$ in the main loop of Q_L and Q_R . The phenomena of vacuum Rabi splitting are observed. By fitting the curves of vacuum Rabi splitting, we can obtain the coupling strengths between cavities and the two qubits.

Data availability

The authors declare that the data supporting the findings of this study are available within the paper and its Supplementary Information files. Source data are provided. Source data are provided with this paper.

References

- Bender, C. M. Making sense of non-Hermitian Hamiltonians. *Rep. Prog. Phys.* **70**, 947-1018 (2007).
- Christodoulides, D. N. & Yang, J. *Parity-time Symmetry and Its Applications*. **280** (Springer, 2018).
- Doppler, J. et al. Dynamically encircling an exceptional point for asymmetric mode switching. *Nature* **537**, 76-79 (2016).
- Dembowski, C. et al. Experimental observation of the topological structure of exceptional points. *Phys. Rev. Lett.* **86**, 787-790 (2001).
- Gao, T. et al. Observation of non-Hermitian degeneracies in a chaotic exciton-polariton billiard. *Nature* **526**, 554-558 (2015).
- Guo, A. et al. Observation of PT -symmetry breaking in complex optical potentials. *Phys. Rev. Lett.* **103**, 093902 (2009).

7. Rüter, C. E. et al. Observation of parity–time symmetry in optics. *Nat. Phys.* **6**, 192–195 (2010).
8. Klaiman, S., Günther, U. & Moiseyev, N. Visualization of branch points in PT-symmetric waveguides. *Phys. Rev. Lett.* **101**, 080402 (2008).
9. Lin, Z. et al. Unidirectional invisibility induced by PT-symmetric periodic structures. *Phys. Rev. Lett.* **106**, 213901 (2011).
10. Regensburger, A. et al. Parity-time synthetic photonic lattices. *Nature* **488**, 167–171 (2012).
11. Peng, B. et al. Parity-time-symmetric whispering-gallery microcavities. *Nat. Phys.* **10**, 394–398 (2014).
12. Chang, L. et al. Parity-time symmetry and variable optical isolation in active-passive-coupled microresonators. *Nat. Photon.* **8**, 524–529 (2014).
13. Peng, B. et al. Chiral modes and directional lasing at exceptional points. *Proc. Natl Acad. Sci.* **113**, 6845–6850 (2016).
14. Peng, B. et al. Loss-induced suppression and revival of lasing. *Science* **346**, 328–332 (2014).
15. Feng, L., Wong, Z. J., Ma, R.-M., Wang, Y. & Zhang, X. Single-mode laser by parity-time symmetry breaking. *Science* **346**, 972–975 (2014).
16. Hodaei, H., Miri, M.-A., Heinrich, M., Christodoulides, D. N. & Khajavikhan, M. Parity-time-symmetric microring lasers. *Science* **346**, 975–978 (2014).
17. Jing, H. et al. PT-symmetry phonon laser. *Phys. Rev. Lett.* **113**, 053604 (2014).
18. Zhang, G.-Q. et al. Exceptional point and cross-relaxation effect in a hybrid quantum system. *PRX Quantum* **2**, 020307 (2021).
19. Wiersig, J. Enhancing the sensitivity of frequency and energy splitting detection by using exceptional points: application to microcavity sensors for single-particle detection. *Phys. Rev. Lett.* **112**, 203901 (2014).
20. Liu, Z.-P. et al. Metrology with PT-symmetric cavities: Enhanced sensitivity near the PT-phase transition. *Phys. Rev. Lett.* **117**, 110802 (2016).
21. Chen, W., Özdemir, S. K., Zhao, G., Wiersig, J. & Yang, L. Exceptional points enhance sensing in an optical microcavity. *Nature* **548**, 192–196 (2017).
22. Hodaei, H. et al. Enhanced sensitivity at higher-order exceptional points. *Nature* **548**, 187–191 (2017).
23. Xu, H., Mason, D., Jiang, L. & Harris, G. E. Topological energy transfer in an optomechanical system with exceptional points. *Nature* **537**, 80 (2016).
24. Naghiloo, M., Abbasi, M., Joglekar, Y. N. & Murch, K. W. Quantum state tomography across the exceptional point in a single dissipative qubit. *Nat. Phys.* **15**, 1232–1236 (2019).
25. Quijandria, F., Naether, U., Ozdemir, S. K., Nori, F. & Zueco, D. PT-symmetric circuit QED. *Phys. Rev. A* **97**, 053846 (2018).
26. Wu, Y. et al. Observation of parity-time symmetry breaking in a single-spin system. *Science* **364**, 878–880 (2019).
27. Ding, L. et al. Experimental determination of PT-symmetric exceptional points in a single trapped ion. *Phys. Rev. Lett.* **126**, 083604 (2021).
28. Klauck, F. et al. Observation of PT-symmetric quantum interference. *Nat. Photon.* **13**, 883–887 (2019).
29. Maraviglia, N. et al. Photonic quantum simulations of coupled PT-symmetric Hamiltonians. *Phys. Rev. Res.* **4**, 013051 (2022).
30. Huang, R., Miranowicz, A., Liao, Jie-Qiao, Nori, F. & Jing, H. Non-reciprocal photon blockade. *Phys. Rev. Lett.* **121**, 153601 (2018).
31. Abdo, B. et al. Active protection of a superconducting qubit with an interferometric Josephson isolator. *Nat. Commun.* **10**, 3154 (2019).
32. Scheucher, M., Hilico, A., Will, E., Volz, J. & Rauschenbeutel, A. Quantum optical circulator controlled by a single chirally coupled atom. *Science* **354**, 2118 (2016).
33. Gu, X., Kockum, A. F., Miranowicz, A., Liu, Y. & Nori, F. Microwave photonics with superconducting quantum circuits. *Phys. Rep.* **718**, 1–102 (2017).
34. Blais, A., Girvin, S. M. & Oliver, W. D. Quantum information processing and quantum optics with circuit quantum electrodynamics. *Nat. Phys.* **16**, 247–256 (2020).
35. Naaman, O., Abutaleb, M. O., Kirby, C. & Rennie, M. On-chip Josephson junction microwave switch. *Appl. Phys. Lett.* **108**, 112601 (2016).
36. Pechal, M. et al. Superconducting switch for fast on-chip routing of quantum microwave fields. *Phys. Rev. Appl.* **6**, 024009 (2016).
37. Wagner, A., Ranzani, L., Ribeill, G. & Ohki, T. A. Demonstration of a superconducting nanowire microwave switch. *Appl. Phys. Lett.* **115**, 172602 (2019).
38. Peng, Z. H., de Graaf, S. E., Tsai, J. S. & Astafiev, O. V. Tuneable on-demand single-photon source in the microwave range. *Nat. Commun.* **7**, 12588 (2016).
39. Kono, S., Koshino, K., Tabuchi, Y., Noguchi, A. & Nakamura, Y. Quantum non-demolition detection of an itinerant microwave photon. *Nat. Phys.* **14**, 546 (2018).
40. Hoi, I. C. et al. Generation of nonclassical microwave states using an artificial atom in 1D open space. *Phys. Rev. Lett.* **108**, 263601 (2012).
41. Magnard, P. et al. Microwave quantum link between superconducting circuits housed in spatially separated cryogenic systems. *Phys. Rev. Lett.* **125**, 260502 (2020).
42. Chen, W., Abbasi, M., Joglekar, Y. N. & Murch, K. W. Quantum jumps in the non-Hermitian dynamics of a superconducting Qubit. *Phys. Rev. Lett.* **127**, 140504 (2021).
43. Gaikwad, C., Kowsari, D., Chen, W. & Murch, K. W. Observing parity-time symmetry breaking in a Josephson parametric amplifier. *Phys. Rev. Res.* **5**, L042024 (2023).
44. Teixeira, W. S., Vadimov, V., Mörstedt, T., Kundu, S. & Möttönen, M. Exceptional-point-assisted entanglement, squeezing, and reset in a chain of three superconducting resonators. *Phys. Rev. Res.* **5**, 033119 (2023).
45. Peng, Z. H. et al. Correlated emission lasing in harmonic oscillators coupled via a single three-level artificial atom. *Phys. Rev. Lett.* **115**, 223603 (2015).
46. Baust, A. et al. Tunable and switchable coupling between two superconducting resonators. *Phys. Rev. B* **91**, 014515 (2015).
47. Dolan, G. J. Offset masks for lift-off photoprocessing. *Appl. Phys. Lett.* **31**, 337–339 (1977).
48. Chen, Z. et al. Fabrication and characterization of aluminum air-bridges for superconducting microwave circuits. *Appl. Phys. Lett.* **104**, 052602 (2014).

Acknowledgements

We thank Long-cheng Gui for help discussions. Devices were made at the Nanofabrication Facilities at the Institute of Physics in Beijing. This work was supported by the National Natural Science Foundation of China under Grant nos. 12074117, 61833010, 62433015, the Innovation Program for Quantum Science and Technology (Grant no. 2021ZD0301800). J.Z. was supported by Laoshan Laboratory (LSKJ202200900), the Leading Scholar of Xi'an Jiaotong University, and the Innovative leading talent project of “Shuangqian plan” in Jiangxi Province. D.Z. was supported by the National Natural Science Foundation of China (Grant nos. 12204528, 92265207, T2121001), and the Micro/nano Fabrication Laboratory of Synergetic Extreme Condition User Facility (SECUF). J.S.T. was supported by the New Energy and Industrial Technology Development Organization (NEDO) under Grant no. JPNP16007. J.H. and L.M.K. were supported by the NSFC under Grant no. 12421005, the XJ-Lab key project, and the STI Program of Hunan Province under Grant no. 2023ZJ1010. F.N. was supported in part by NTT Research, JST (via the Q-LEAP program, and the Moonshot R&D Grant Number JPMJMS2061), AOARD (Grant no. FA2386-20-1-4069), and ONR.

Author contributions

Y.X.L., J.Z., and Z.P. conceived the idea. P.S., D.Z. and Z.P. designed the experiments. P.S. fabricated the device. P.S. and X.R. performed the experiments and processed the data. X.R. provided a theoretical analysis. Y.X.L., J.Z., H.J. and F.N. guided the theory. J.S.T. and L.Y. guided the experiments. J.Z. and Z.P. wrote the main text with contributions from all authors. P.S. and X.R. wrote the supplementary materials with contributions from all authors. H.D., S.L., M.C., R.H., L.M.K., and Q.Z. provided some technical support. Z.P. supervised the project.

Competing interests

The authors declare no competing interests.

Additional information

Supplementary information The online version contains supplementary material available at

<https://doi.org/10.1038/s41467-024-54199-w>.

Correspondence and requests for materials should be addressed to Dongning Zheng, Jing Zhang or Zhihui Peng.

Peer review information *Nature Communications* thanks the anonymous reviewer(s) for their contribution to the peer review of this work. A peer review file is available.

Reprints and permissions information is available at

<http://www.nature.com/reprints>

Publisher's note Springer Nature remains neutral with regard to jurisdictional claims in published maps and institutional affiliations.

Open Access This article is licensed under a Creative Commons Attribution-NonCommercial-NoDerivatives 4.0 International License, which permits any non-commercial use, sharing, distribution and reproduction in any medium or format, as long as you give appropriate credit to the original author(s) and the source, provide a link to the Creative Commons licence, and indicate if you modified the licensed material. You do not have permission under this licence to share adapted material derived from this article or parts of it. The images or other third party material in this article are included in the article's Creative Commons licence, unless indicated otherwise in a credit line to the material. If material is not included in the article's Creative Commons licence and your intended use is not permitted by statutory regulation or exceeds the permitted use, you will need to obtain permission directly from the copyright holder. To view a copy of this licence, visit <http://creativecommons.org/licenses/by-nc-nd/4.0/>.

© The Author(s) 2024